

Efficient thermal rectification in nitrogen-doped carbon nanotube heterostructures

Zhibo Xing(邢志博), Yingguang Liu(刘英光), Haochen Liu(刘浩宸), Yahao Wang(王雅浩), Cheng Zhang(张成), and Ning Wu(吴宁)

Citation: Chin. Phys. B, 2025, 34 (**11**): 116101. DOI: 10.1088/1674-1056/adfdc4
http://cpb.iphy.ac.cn; http://iopscience.iop.org/cpb

What follows is a list of articles you may be interested in

Improved temperature localization by hollowing plasmonic nanofocusing cones

Jiaming Zhang(张家明) and Jinglai Duan(段敬来)
Chin. Phys. B, 2025, 34 (**6**): 066104. DOI: 10.1088/1674-1056/adc409

Effect of copper/tungsten heterophase interface on radiation resistance: Insights from atomistic simulations

Wen Chen(陈文), Min Li(李敏), Bao-Qin Fu(付宝勤), Tun Chen(陈暾), Jie-Chao Cui(崔节超), and Qing Hou(侯氢)
Chin. Phys. B, 2025, 34 (**4**): 046108. DOI: 10.1088/1674-1056/adb40d

Design and preparation of amorphous carbon nanotubes reinforced copper

Xiaona Ren(任晓娜), Wentao Wu(吴文涛), Zhipei Chen(陈志培), and Changchun Ge(葛昌纯)
Chin. Phys. B, 2025, 34 (**4**): 046107. DOI: 10.1088/1674-1056/adb8b7

Influence of nitrogen and magnesium doping on the properties of ZnO films

Dong-hua Li(李东华), Hui-Qiong Wang(王惠琼), Hua Zhou(周华), Ya-Ping Li(李亚平), Zheng Huang(黄政), Jin-Cheng Zheng(郑金成), Jia-Ou Wang(王嘉鸥), Hai-jie Qian(钱海杰), Kurash Ibrahim(奎热西), Xiaohang Chen(陈晓航), Huahan Zhan(詹华瀚), Yinghui Zhou(周颖慧), Junyong Kang(康俊勇)
Chin. Phys. B, 2016, 25 (**7**): 076105. DOI: 10.1088/1674-1056/25/7/076105

Comparative study on beryllium and magnesium as a co-doping element for ZnO:N

Yu-Quan Su(苏宇泉), Ming-Ming Chen(陈明明), Long-Xing Su(苏龙兴), Yuan Zhu(祝渊), Zi-Kang Tang(汤子康)
Chin. Phys. B, 2016, 25 (**6**): 066106. DOI: 10.1088/1674-1056/25/6/066106

SPECIAL TOPIC — Heat conduction and its related interdisciplinary areas

Efficient thermal rectification in nitrogen-doped carbon nanotube heterostructures

Zhibo Xing(邢志博)[1], Yingguang Liu(刘英光)[1,2,†], Haochen Liu(刘浩宸)[1], Yahao Wang(王雅浩)[1], Cheng Zhang(张成)[1], and Ning Wu(吴宁)[1]

[1] *Department of Power Engineering, School of Energy and Power Engineering, North China Electric Power University, Baoding* 071003, *China*
[2] *Hebei Key Laboratory of Low Carbon and High Efficiency Power Generation Technology, North China Electric Power University, Baoding* 071003, *China*

(Received 27 May 2025; revised manuscript received 15 August 2025; accepted manuscript online 21 August 2025)

Carbon nanotubes (CNTs) are widely used in various fields owing to their unique properties. In this study, three different types of nitrogen-doped CNT heterojunctions were constructed: parallel-doped (PCNT), vertically doped (VCNT), and mesh-doped (MCNT). Non-equilibrium molecular dynamics (NEMD) simulations were conducted to investigate their heat flux and thermal rectification (TR) effects. The results show that heat flux preferentially flows from nitrogen-doped regions to undoped regions, exhibiting distinct thermal rectification behavior, with PCNT showing the most pronounced effect. Interestingly, the TR ratio of the zigzag PCNT is significantly higher than that of the armchair PCNT. Subsequently, we examined the effects of system length and diameter on the TR ratio of the PCNT and found that the TR ratio increases and then decreases with increasing model length. In addition, the effect of defect density on the heat flux of the PCNT is peculiar. The phonon density of states, phonon dispersion, participation ratio, and phonon spectral heat flux were analyzed to elucidate the thermal transport behavior of phonons in the nanotubes. This study provides insights into the development and design of nitrogen-doped CNT thermal rectifiers.

Keywords: carbon nanotube heterojunction, nitrogen doping, thermal rectification, nonequilibrium molecular dynamics

PACS: 61.46.–w, 65.80.–g, 44.10.+i, 31.15.xv, 47.61.–k

DOI: 10.1088/1674-1056/adfdc4 **CSTR:** 32038.14.CPB.adfdc4

1. Introduction

The field of micro/nanotechnology has expanded substantially in recent decades, leading to the development of diverse thermal management devices. Notably, such devices, akin to electric diodes, have garnered considerable attention. Thermal rectification (TR) — the facilitation of easier heat transfer in one direction than in the opposite — has become a focal point of research. The origins of this concept trace back to Starr's pioneering experimental observation in 1936.[1] Since then, experimental and theoretical research has progressed rapidly, with major studies focusing on thermal diodes,[2–4] thermal transistors,[5] and further extending to intelligent thermal management systems as well as thermoelectric and thermal storage materials.[6,7] Initially, research on thermally rectified materials was concentrated on macroscopic scales.[8,9] However, advances in nanomaterials and nanotechnologies have revealed their superior TR properties compared with macroscopic materials. Achieving such properties in nanomaterials typically involves the creation of asymmetric structures,[10–12] the introduction of defects and doping,[13,14] and the application of functionalization techniques.[15] The TR phenomena observed in these studies can be attributed to mismatches in phonon vibrational spectra,[11,16–18] localized phonon resonances,[12,19] and standing wave effects.[20] Guided by these fundamental principles, researchers have successfully engineered numerous nanoscale thermal rectifiers with outstanding performance, such as triangular cone diamond structures,[16] silicon nanowires,[17] gradient core–shell nanowires,[20] nano-heterojunctions,[11,18,21] and phase change materials.[22,23] Nevertheless, it is important to recognize that while these materials exhibit promise, they currently do not demonstrate exceptional rectification ratios or heat transfer efficiencies. Consequently, the focus of thermal rectifier development has shifted toward materials exhibiting both high thermal conductivity and strong rectification performance.

At the same time, carbon nanotubes (CNTs), discovered by Iijima in 1991,[24] have attracted significant research interest. Currently, two primary strategies exist for achieving efficient TR using carbon-based materials such as graphene and CNTs. One approach involves constructing heterogeneous structures, which can be integrated in multiple ways. For instance, CNT arrays can serve as thermal interface materials filling gaps between chips and heat sinks, heat sinks and radiators, or chips and packaging substrates. They can also be

[†]Corresponding author. E-mail: yingguang266@126.com

© 2025 Chinese Physical Society and IOP Publishing Ltd. All rights, including for text and data mining, AI training, and similar technologies, are reserved.

incorporated beneath, above, or near the source/drain extension area of the gate dielectric layer in transistors to reduce peak channel temperatures. Aiyiti *et al.*[25] experimentally investigated the TR effect of Y-junction CNTs and found that a TR ratio of approximately 8.3% can be achieved under a small temperature difference (4 K). This effect arises from new optical phonon modes generated by interlayer van der Waals interactions in multi-walled CNT regions, leading to asymmetric phonon propagation in the high-frequency range. Similarly, Chen *et al.*[26] observed a TR ratio of up to 334% in CNT/hexagonal boron nitride nanotube (BNNT) heterojunctions. By analyzing phonon mode distributions, they found that during forward heat flow, most atoms in the CNT region participate in thermal vibration, whereas under backward heat flow, atomic vibration in this region is minimal, thereby elucidating the TR phenomenon. Moreover, Zhuang *et al.*[27] demonstrated that tuning the boundary structure in graphene/boron nitride heterojunctions significantly enhances the TR ratio. This enhancement stems from asymmetric heat flux caused by differences in the overlap of phonon state densities at graphene and boron nitride interfaces under forward and backward heat flow. Another effective strategy involves introducing asymmetric doping of foreign atoms. For example, Yang *et al.*[28] proposed two nitrogen-doped graphene nanoribbon models, single (SNDG) and vertical (VNDG) doping configurations, and found that the TR ratio of SNDG decreased with increasing temperature, whereas that of VNDG remained constant. In a subsequent study, Yang *et al.*[14] investigated the thermal properties of triangular nitrogen-doped graphene nanoribbons and found that the TR ratio increased with nitrogen concentration. They observed that the incorporation of nitrogen atoms expanded the asymmetric interfacial region, resulting in a greater difference in heat flux between forward and backward directions. However, studies on modulating the TR of CNTs through nitrogen doping remain relatively limited.[29]

To further advance understanding, we constructed three CNT heterojunctions with distinct nitrogen-doping configurations: parallel-doped (PCNT), vertically doped (VCNT), and mesh-doped (MCNT). Using nonequilibrium molecular dynamics (NEMD) simulations, we investigated the interfacial heat transport mechanisms in these three models. Moreover, Han *et al.*[30] have demonstrated the feasibility of fabricating such heterojunctions, providing experimental support for our simulations. The chirality of the CNTs selected for the initial model is $(n,0)$. Our results reveal that heat flux preferentially flows from the nitrogen-doped region to the undoped region in all three models, with the PCNT exhibiting the highest TR ratio. Accordingly, subsequent discussions focus on the PCNT and explore the effects of temperature difference, size, and defects on the TR ratio. These findings offer valuable insights into the design of thermal rectifiers, intelligent thermal management systems, and microelectronic cooling devices.

2. Structure and computational methodology

Three different types of nitrogen-doped graphene sheets and their corresponding rolled nitrogen-doped CNTs are shown in Figs. 1(a)–1(c), respectively. The three nitrogen-doped configurations of graphene selected here are consistent with our previous work.[31] The chirality of the CNTs chosen for the initial model is $(n,0)$, and after structural optimization, we used a model with $n = 18$. The total length of the model is 17 nm, the diameter is 1.4 nm, and the vacuum layer is defined as a coaxial region surrounding the CNTs with a cross-sectional area of 2×2 nm^2, the length of which equals that of the model. To maintain structural stability during the simulation, fixed boundary conditions were applied at positions 1 nm from both the right and left ends of the model. These constraints prevented rotation and ensured the model remained stationary. The gray-shaded areas in Fig. 1 represent these fixed regions, while periodic boundary conditions were applied in the other two directions. To establish irreversible heat flux during the simulation, the intermediate region, excluding the fixed regions, was divided into 50 layers. The regions six layers away from each of the left and right fixed regions were designated as hot and cold baths, maintained at temperatures T_h and T_l, respectively. These are shown by the red and blue dashed sections in Fig. 1

$$T_\mathrm{h} = T(1+\Delta), \tag{1}$$

$$T_\mathrm{l} = T(1-\Delta), \tag{2}$$

where T is the ambient temperature, and Δ is the temperature difference.

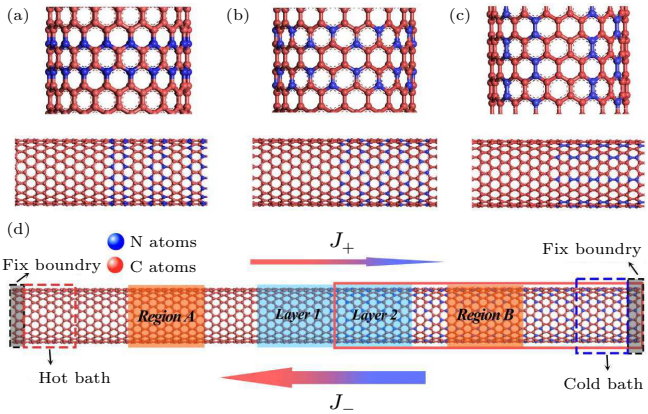


Fig. 1. Schematic models of three nitrogen-doped CNT heterostructures: (a) vertical doping of CNT (VCNT), (b) mesh doping of CNT (MCNT), (c) parallel doping of CNT (PCNT), and (d) perspective view of the atomic model of the mesh-doped CNT heterostructure (MCNT). Hot and cold baths are applied at both ends of the simulated system (excluding the fixed layer of 1 nm), generating a heat flux across the interface.

In this study, we utilized non-equilibrium molecular dynamics (NEMD) simulations performed using the Large-Scale

Atomic/Molecular Massively Parallel Simulator (LAMMPS) package.[32] Following the approach outlined by Ghasemi and Cheng *et al.*,[33,34] an optimized Tersoff potential function was employed to accurately describe the force constants between C–C and C–N atoms in the model. The simulation procedure comprised four main steps. (1) With a time step of 0.5 fs, the model was first placed in the NPT ensemble for 500 ps of relaxation to obtain an optimized structure. (2) The system was then equilibrated in a Nosé–Hoover[35] NPT heat bath at ambient temperature T for 500 ps to maintain temperature control. (3) Considering the potential instability of the Nosé–Hoover thermostat, the hot and cold baths were subsequently controlled using a Berendsen[36] heat bath. (4) Finally, the model was placed in the NVE ensemble and run for 1.2×10^7 steps to calculate the heat flux. It should be noted that the heat bath coupling parameter τ was set to 100 fs, and the heat bath layer thickness was set to 10 Å. Specifically, we tested the effects of τ and heat bath layer thickness on heat flux and TR ratio and found that a smaller τ (50 fs) accelerates relaxation but may cause slight over-damping of temperature, while a larger τ (500 fs) significantly prolongs relaxation. However, the change in heat flux remained within $\pm6\%$, and the forward and backward heat flux trends were consistent. Most importantly, the TR ratio varied minimally within the tested τ range. A thinner heat bath layer (5 Å) slightly increased temperature fluctuations in the thermal bath region, whereas a thicker layer (20 Å) mildly suppressed atomic vibrations near the boundary. Nevertheless, the ratio of forward to backward heat flux remained similar, resulting in a highly stable calculated TR ratio. For each simulated system, six independent runs were performed, and the averaged values were reported in the figures. Furthermore, simulation conditions were kept consistent across all cases unless otherwise specified. These included a temperature of 300 K, a model length of 17 nm, a chirality of (18,0), an inner diameter of 1.4 nm, and a Δ value of 0.3.

The heat flux from the undoped region to the nitrogen-doped region is denoted as J_+, and the backward heat flux as J_-. The heat flux density of the system, J, can be calculated from the energy exchange rate in the heat source and sink regions as follows:

$$J=\left(\frac{\partial E_{\text{hot}}}{\partial t}+\frac{\partial E_{\text{cold}}}{\partial t}\right)/(2A), \tag{3}$$

where E_{hot} and E_{cold} represent the energy gained by the hot bath and removed from the cold bath, respectively, and A is the cross-sectional area of the simulation system perpendicular to the heat transfer direction. The TR ratio was calculated using the following equation:

$$\eta=\frac{J_- - J_+}{J_-}\times100\%. \tag{4}$$

3. Results and discussion

3.1. Effect of temperature on TR of three nitrogen-doped models

Initially, the forward and backward heat fluxes of the models were obtained through NEMD simulations, with the ambient temperature T set to 300 K, the temperature difference Δ to 120 K, the system length L to 17 nm, and the chirality of the heterogeneous nanotubes fixed at (18,0). The temperature distribution along the heterogeneous nanotube was calculated according to

$$T=\frac{1}{3Nk_{\text{B}}}\sum_{i=1}^{N}m_i v_i^2, \tag{5}$$

where N is the total number of atoms in the heterogeneous nanotube, k_{B} is the Boltzmann constant, and m_i and v_i are the mass and velocity of atom i, respectively. Based on Eq. (5), the temperature distributions of the heterogeneous nanotube for forward and backward heat fluxes are shown in Fig. 2(d). The dependence of the heat flux magnitude and TR rate on the ambient temperature T for the three models is illustrated in Fig. 2.

In Fig. 2(a), to distinguish between the forward and backward heat fluxes, the ambient temperatures corresponding to the forward and backward heat fluxes are denoted as T_{f} and T_{b}, respectively. Across all three models, J_- consistently exceeds J_+, indicating a dominant heat flow from the nitrogen-doped region toward the undoped region. This observation is consistent with previous research.[26] The heat flux values for all three models increase with rising average temperature. Figure 2(b) further shows that the TR rate decreases with increasing ambient temperature in all three models. This trend can be attributed to the progressive enhancement of phonon–phonon scattering at elevated temperatures, which weakens the asymmetry between forward and backward heat fluxes.

Notably, at an average temperature of 300 K, the PCNT exhibits the highest TR rate of 213.15%, surpassing both VCNT and MCNT, which highlights its superior performance as a thermal rectifier at room temperature. However, the TR rate of PCNT is highly sensitive to temperature variations, rapidly dropping to 3.05% as the temperature rises to 600 K. In contrast, the TR rates of VCNT and MCNT decline more gradually, with the latter maintaining a relatively higher TR across the entire temperature range. Even at 600 K, the TR rate of MCNT remains as high as 75%, indicating its excellent rectification capability at elevated temperatures.

Currently, several studies have investigated the TR performance of two-dimensional planar graphene/C_3N heterojunctions. For example, Song *et al.*[37] reported a TR rate of 13.77% in graphene/C_3N heterojunctions, while Farzadian *et al.*[38] achieved a TR rate of only 50% even under a large temperature difference ($\Delta T=100$ K). To further compare and evaluate the difference in TR strength

betweentwo-dimensional graphene and one-dimensional carbon nanotubes, we constructed and analyzed heterojunction models with identical nitrogen-doping configurations: parallel doping of graphene (PGR), vertical doping of graphene (VGR), and mesh doping of graphene (MGR). The TR performance indices obtained under identical simulation parameters for all systems are presented in Fig. 2(c). The results reveal that the TR ratios of the nitrogen-doped graphene models are significantly limited at all temperatures.

To further investigate the effects of different nitrogen-doping configurations on the phonon vibrational modes of CNTs, we calculated the dispersion curves for three nitrogen-doped forms, as well as for undoped pure CNTs. These were obtained by performing a two-dimensional Fourier transform on the time history of the velocity field,[39] which can be expressed as

$$\phi(k,\omega) = \left| \frac{1}{N} \int v_\alpha \exp(\mathrm{i}ky - \mathrm{i}\omega t)\,\mathrm{d}t\,\mathrm{d}y \right|, \quad (\alpha = x,y,z), \tag{6}$$

where N is the number of atoms in the system, y is the heat conduction direction, k is the wave vector, and ω is the phonon frequency. The velocity component v_α is projected onto the x, y, and z directions to calculate the phonon energy densities for the individual phonon modes. The calculated results are shown in Fig. 3(a). To further analyze the dispersion relation, the dispersion curves were differentiated to obtain the phonon group velocities, as depicted in Fig. 3(b).

By considering the group velocity and dispersion relations, it can be inferred that phonon localization in undoped CNTs is minimal. Moreover, the parallel-doped region exhibits the flattest dispersion profile. A distinct band gap is also visible in the region marked by a dashed box. Within this region, the interaction between the flat and non-flat bands induces the coupling of local resonance phonon modes with normal propagating phonon modes, leading to the formation of high-intensity local resonances. This mechanism significantly suppresses heat flux.[40] Consequently, parallel doping results in the smallest phonon group velocity and the lowest heat flux.

It is worth noting that in all three nitrogen-doping models, when heat flux proceeds from the left end to the right end, that is, from the non-flat-band region to the flat-band region, most of the frequency range of the non-flat-band region does not overlap with that of the flat-band region, making it difficult for phonons to traverse the interface. Conversely, for backward heat flux, phonons can pass through the interface more easily, resulting in different interfacial thermal resistances for forward and backward heat fluxes. Therefore, the backward heat flux exceeds the forward heat flux. Furthermore, the larger the proportion of the flat region in the dispersion curve of the nitrogen-doped segment, the more pronounced the difference in interfacial thermal resistance between the forward and backward heat fluxes, leading to a higher TR ratio. Consequently, PCNT exhibits the most significant TR effect at room temperature, while VCNT shows a weaker TR effect.

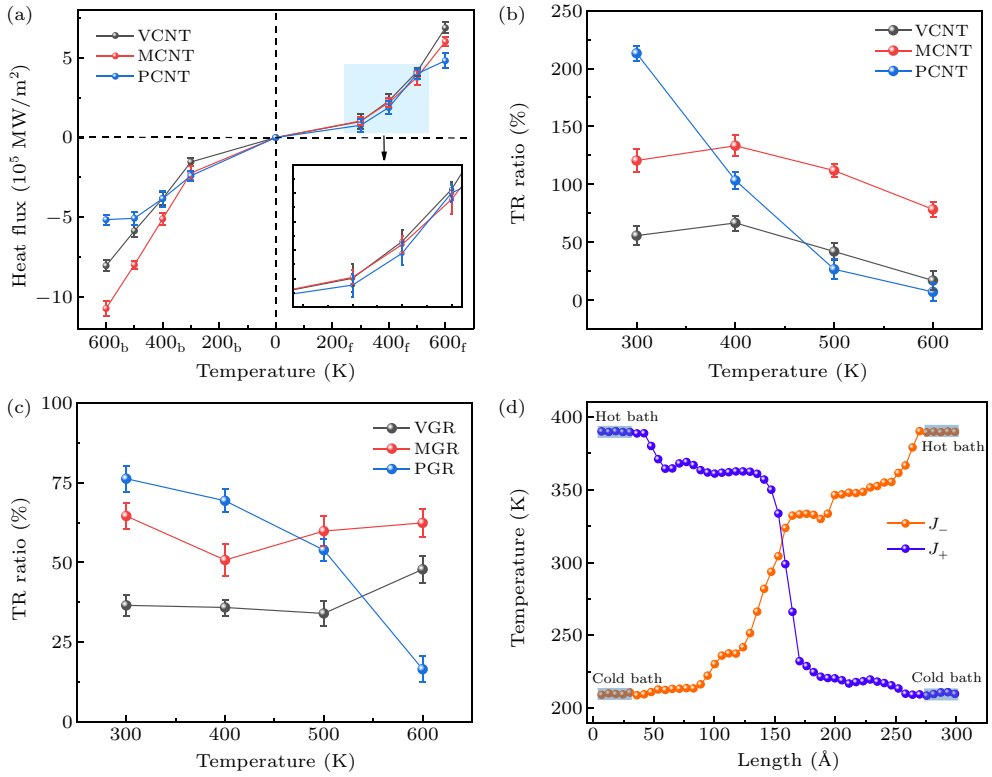


Fig. 2. The effect of temperature on (a) the heat flux and (b) the TR ratio for VCNT, MCNT, and PCNT; (c) the TR ratio for VGR, MGR, and PGR; and (d) the local temperature distribution under forward and backward heat fluxes in PCNT.

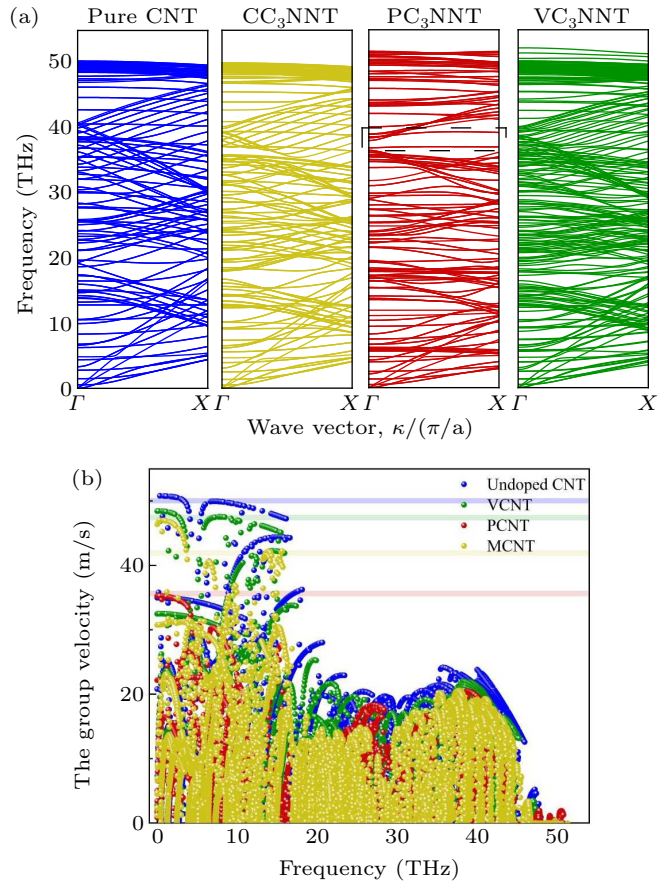


Fig. 3. The effect of different nitrogen doping forms on (a) the dispersion curves and (b) the group velocity.

To further visualize the phonon heat transfer characteristics, we calculated the phonon density of states (PDOS) for each of the three models and discussed them in detail.

The PDOS along the heat flux direction was obtained by performing a Fourier transform on the velocity autocorrelation function (VACF),[41] as given by

$$\mathrm{PDOS}(\omega) = \frac{1}{\sqrt{2\pi}} \int_{-\infty}^{+\infty} \mathrm{e}^{\mathrm{i}\omega t} \frac{1}{N} \left\langle \sum_{i=1}^{N} v_i(t) v_i(0) \right\rangle \mathrm{d}t, \quad (7)$$

where $\boldsymbol{v}_i(0)$ denotes the mean velocity vector of particle i at the initial moment, $\boldsymbol{v}_i(t)$ denotes that at time t, ω represents the vibration frequency, and the angle brackets indicate the ensemble average.

To quantify the degree of spectral matching between different regions under forward and backward heat flux, we calculated the overlap of the PDOS based on the theory of density-of-states overlap[42]

$$S_{\pm} = \int_0^{\infty} \min\{P_1(\omega), P_2(\omega)\} \mathrm{d}\omega, \quad (8)$$

where $P_1(\omega)$ and $P_2(\omega)$ are the PDOS of regions A and B, respectively. The subscripts "+" and "−" represent the forward and backward heat flux directions. The in-plane and out-of-plane PDOS overlaps are defined as S_{I} and S_{O}, respectively. The in-plane PDOS at 300 K was calculated for the three models, as shown in Figs. 4(a)–4(f).

From Fig. 4, it is evident that in the in-plane direction, the overlap of PDOS curves under backward heat flux is greater than that under forward flux for all three nitrogen-doping models. This indicates that heat flow from region B to region A experiences lower thermal resistance, resulting in higher heat flux in the backward direction. However, the differences in PDOS overlap between the forward and backward cases are not substantial. The VCNT exhibits the largest in-plane phonon overlap in both directions, suggesting that it should exhibit the highest forward and backward heat fluxes at $T = 300$ K. However, this observation contradicts the data presented in Fig. 2. Therefore, it is necessary to examine the out-of-plane phonon vibrational modes in regions A and B of the three models, as shown in Figs. 4(a)–4(f). Analyzing these vibrational modes provides additional insights into the observed TR behavior and helps reconcile the discrepancies between the expected and observed heat flux patterns.

As depicted in Fig. 5, consistent with the in-plane PDOS, the overlap of the PDOS corresponding to the backward heat flux surpasses that of the forward heat flux for all three models. Furthermore, the overlap between the forward and backward out-of-plane PDOS of the three models exhibited notable differences, with S/S_+ values of 1.02, 1.03, and 1.071 for VCNT, MCNT, and PCNT, respectively. Moreover, S/S_+ values were calculated for the three models at temperatures of 300 K and 400 K, yielding values of 1.033, 1.054, 1.04, and 1.015, 1.023, 1.01, respectively. These values, along with their respective comparisons of TR rates, are illustrated in Fig. 6. The figure elucidates that the disparity between the forward and backward heat fluxes of the PCNT is most pronounced at 300 K. This suggests that the TR rate reaches its peak at this temperature. Similarly, the ratios of S/S_+ and TR rates for the other two models first increase and then decrease with temperature. Apparently, the ratio of the overlap of forward and backward heat flux shows the same trend as the TR rate as the temperature rises. This observation suggests that out-of-plane phonon transport plays a decisive role in the heat flux and TR rate of the model. Considering the absolute advantage of the TR of PCNT at 300 K, our subsequent study focuses on PCNT.

To explore the effects of sawtooth and armchair shapes on the heat flux and TR rate of the model, we analyzed the dependence of the heat flux on the temperature difference Δ for the zigzag PCNT (ZPCNT) and the armchair PCNT (APCNT), as depicted in Fig. 7(a). Initially, in both cases, the heat flux preferentially flows from the nitrogen-doped region to the non-doped region, exhibiting a significant TR effect, consistent with the aforementioned analysis. Furthermore, the TR rate increases as the magnitude of $|\Delta|$ increases, aligning with the findings of Chen *et al.*[11] and Yang *et al.*[43] When $\Delta < 0$, the heat flux increases rapidly with $|\Delta|$ for both models. However, when $\Delta > 0$, the increase in heat flux of ZPCNT is notably

slower than that of APCNT, particularly for large temperature deviations. To delve deeper into the underlying mechanisms driving these differences, we employed Eq. (9) to calculate the phonon participation rate (PPR) for both models under forward heat flux

$$\mathrm{PPR}(\omega)=\frac{1}{N}\frac{\left[\sum_i\left(\int \mathrm{e}^{\mathrm{i}\omega t}\frac{1}{N}\sum_{i=1}^{N}\langle v_i(0)v_i(t)\rangle\,\mathrm{d}t\right)^2\right]^2}{\sum_i\left(\int \mathrm{e}^{\mathrm{i}\omega t}\frac{1}{N}\sum_{i=1}^{N}\langle v_i(0)v_i(t)\rangle\,\mathrm{d}t\right)^4}. \quad (9)$$

These vectors measure the proportion of atoms participating in a given mode and can effectively indicate a localized mode for $\mathscr{O}(1/N)$ and an off-delocalized mode for $\mathscr{O}(1)$.[44] The results are depicted in Fig. 7(c). It is evident that ZPCNT exhibits a significantly lower phonon participation rate across the majority of frequencies compared to APCNT. This discrepancy can be attributed to the more pronounced boundary scattering characteristic of the zigzag configuration in contrast to the armchair type, causing the transition of too many delocalized phonons to localized ones, which leads to a lower heat flux. Furthermore, we calculated the dispersion curves and group velocities of both ZPCNT and APCNT using Eq. (6), as illustrated in Figs. 7(d) and 7(e). A clear distinction is observed: ZPCNT features a flatter dispersion profile, and its group velocity is substantially lower than that of APCNT across almost the entire frequency range. This indicates that ZPCNT harbors a higher proportion of localized phonon modes. Meanwhile, the local phonons are not affected by temperature, so the forward heat flux of the ZPCNT does not significantly increase with temperature difference. However, the APCNT, with a higher proportion of off-delocalized phonons, exhibits a more sensitive temperature dependence. Correspondingly, the TR ratio of the ZPCNT grows faster than that of the APCNT as Δ increases. At $\Delta=0.5$, ZPCNT can reach 342%, while APCNT is only 45.92%.

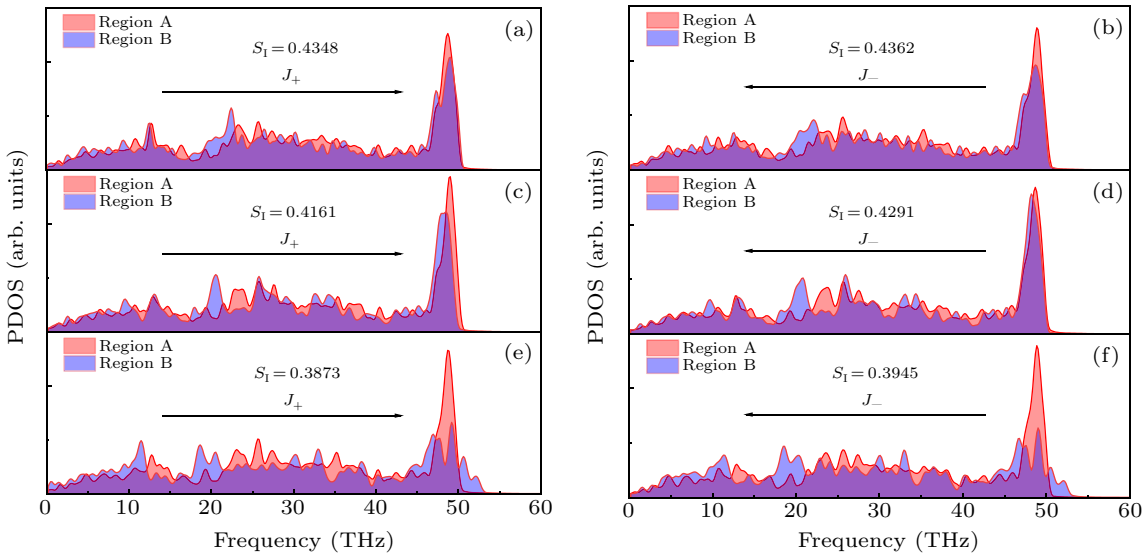


Fig. 4. In-plane PDOS of VCNT ((a) and (b)), MCNT ((c) and (d)), and PCNT ((e) and (f)) at 300 K.

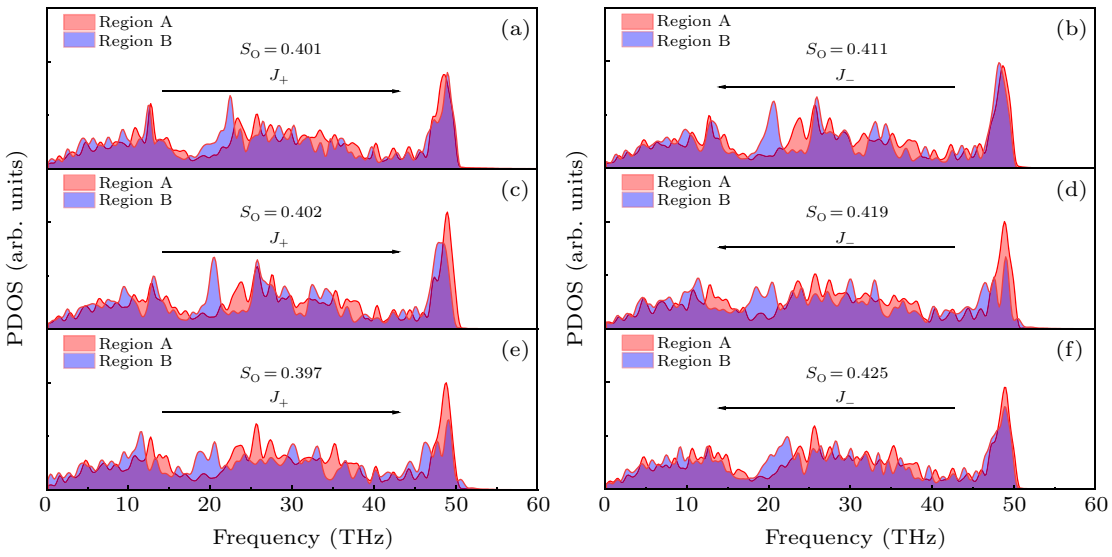


Fig. 5. Out-of-plane PDOS of VCNT ((a) and (b)), MCNT ((c) and (d)), and PCNT ((e) and (f)) at 300 K.

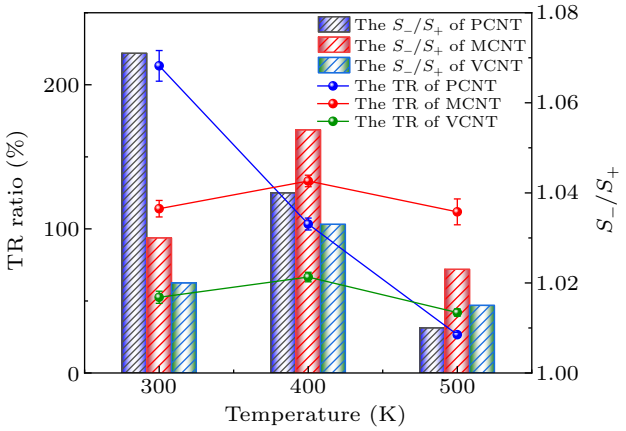


Fig. 6. Ratios of S_-/S_+ and TR ratio of PCNT as a function of temperature.

3.2. Effects of size

At the nanoscale, where the model size is comparable to the phonon mean free path, even subtle dimensional alterations in a model can impact its heat transport properties. Therefore, it is imperative to investigate the influence of size on the TR ratio of the model. In this context, we explore the effects of the length L of heteronanotubes and the diameter W of the tubes on the TR rate of PCNT. As illustrated in Fig. 8(a), with the increase in length, J_+ remains almost constant initially, while J_- experiences rapid growth. Subsequently, when L surpasses 12 nm, J_+ undergoes a sudden increase, whereas J_- stabilizes. The TR ratio, calculated using Eq. (2), is depicted in Fig. 8(a), reaching its peak at $L = 12$ nm before declining rapidly. For instance, TR = 219%, 367%, and 50% when $L = 4$ nm, 12 nm, and 30 nm, respectively. To provide a more comprehensive understanding of the variations in heat flux and TR ratio, we conducted calculations on the PDOS inside the PCNT, and the results are presented in Fig. 9(a). It is clear that the 30 nm model exhibits a greater percentage of PDOS in the low-frequency range compared to the 4 nm and 12 nm models. In the high-frequency region, however, there is no significant difference among the three. When the length of the heteronanotube becomes

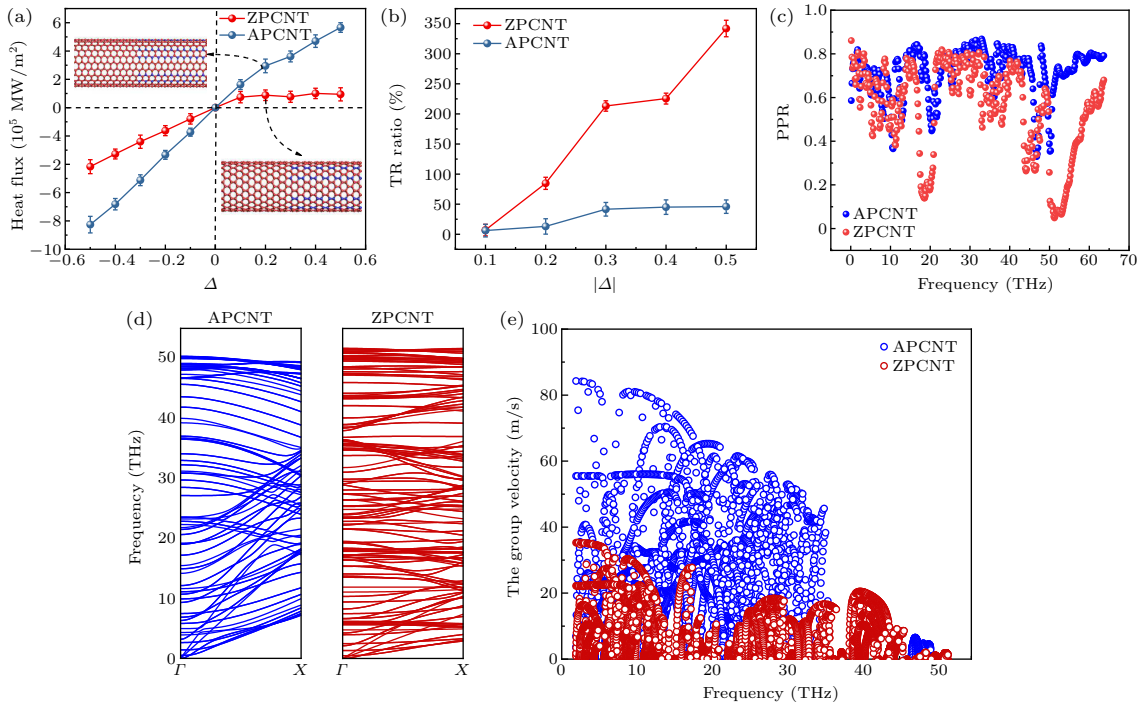


Fig. 7. Effect of temperature difference Δ on (a) heat flux and (b) TR rate of ZPCNT and APCNT; (c) phonon participation rates of ZPCNT and APCNT under forward heat flux; (d) dispersion curves; and (e) group velocities of ZPCNT and APCNT.

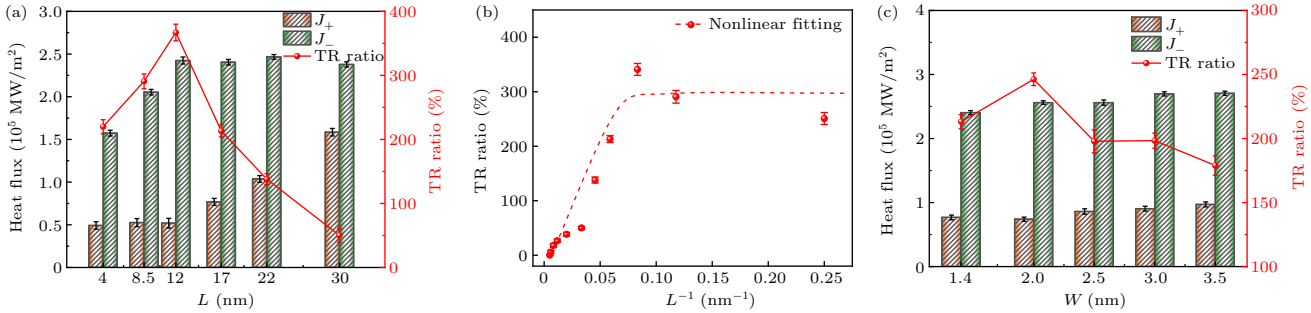


Fig. 8. (a) Heat flux and TR ratio as a function of length. (b) TR ratio as a function of the inverse of the length. (c) Heat flux and TR ratio as a function of the diameter.

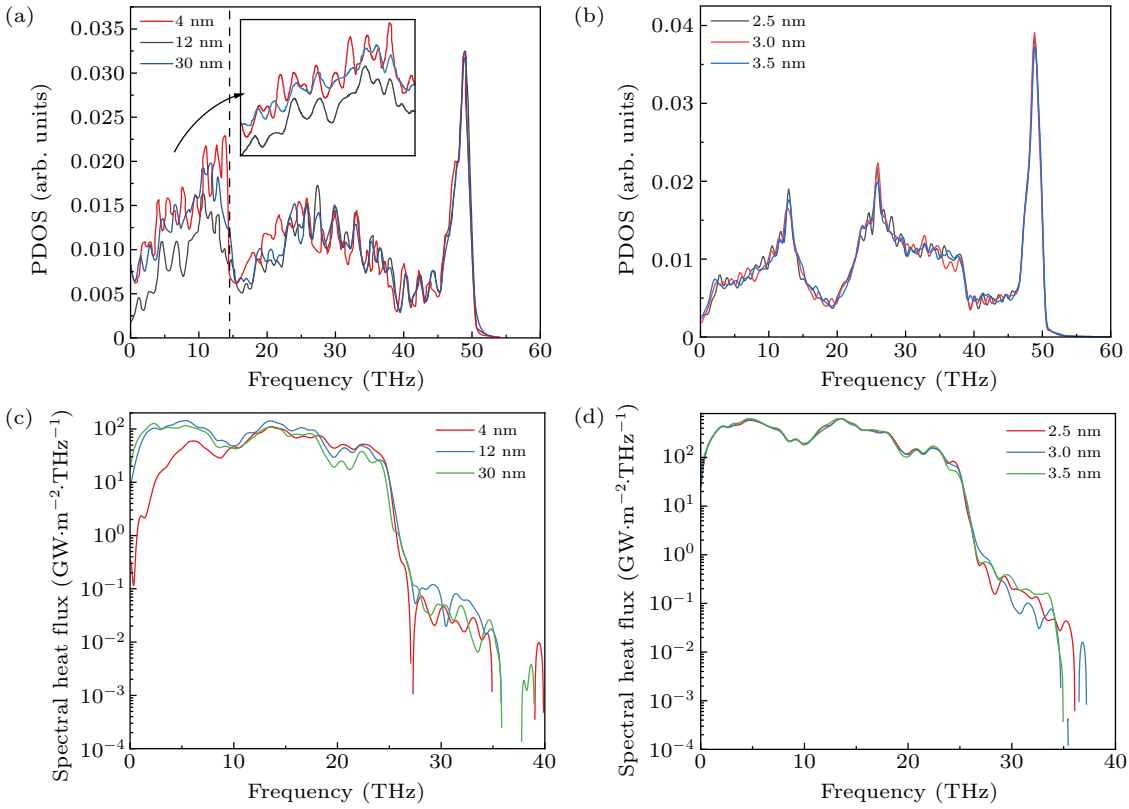


Fig. 9. Comparison of the PDOS of PCNT with lengths of 4 nm, 12 nm, and 30 nm (a), and diameters of 2.5 nm, 3.0 nm, and 3.5 nm (b). Spectral heat flux of PCNT with lengths of 4 nm, 12 nm, and 30 nm (c), and diameters of 2.5 nm, 3.0 nm, and 3.5 nm (d).

further increased, more long-wave phonons transferring across the interface are easily excited, which reduces the difference in forward and backward heat fluxes and weakens the TR ratio. This is consistent with Refs. [26,45–47]. In addition, to more clearly show the TR effect of the model at a large length, we plotted rectification as a function of the inverse of the length, as shown in Fig. 8(b). It can be seen that the model does not have an obvious TR effect at a large scale, which further proves our conclusion.

In order to investigate the effect of length on the involvement of low-frequency phonons in thermal transport, we calculated its spectral heat flux using Eq. (9). When the heat flux is close to the steady state, we respectively take the atoms in layer 1 and layer 2 (as shown in the blue shaded regions in Fig. 1, respectively) in the J_+ direction. The spectral heat flux at these positions is calculated as[48–50]

$$q_{i\to j}(\omega) = -\frac{2}{\omega t}\sum_{\alpha,\beta\in(x,y)} \mathrm{Im}\left\langle \tilde{v}_i^{\alpha}(\omega)^* K_{ij}^{\alpha\beta}\tilde{v}_j^{\beta}(\omega)\right\rangle, \quad (10)$$

where ω is the angular frequency, t is the simulation time, $K_{ij}^{\alpha\beta}$ is the second-order interatomic force constant, and $\tilde{v}_i^{\alpha}(\omega)$ and $\tilde{v}_j^{\beta}(\omega)$ are the discrete Fourier-transformed velocities of atoms i in direction α and atoms j in direction β, respectively. The sum of the heat flux of the atoms in layers 1 and 2, divided by the cross-sectional area, is the spectral heat through the structure, expressed as

$$q(\omega) = \frac{1}{A}\sum_{i\in L}\sum_{j\in R} q_{i\to j}(\omega). \quad (11)$$

Figure 9(c) displays the spectral heat flux calculated using Eqs. (10) and (11). As previously mentioned for PDOS, an increase in length stimulates more low-frequency, long-wavelength phonon modes to participate in thermal transport. Therefore, the effect of the increased length in Fig. 8(a) can be attributed to the fact that the increase in model length excites more long-wave phonons, which are more likely to pass through the doped region and thus contribute to the heat flux. On the other hand, the increase in model length is accompanied by an increase in the number of nitrogen atoms, which enhances phonon scattering at nitrogen-doped sites, thereby suppressing the heat flux to some extent. It is the alternating influence of these two factors that causes the forward and backward heat flux to increase asynchronously, so that the TR rate does not show a linear decrease.

Subsequently, we explored the effect of the model diameter W on the heat flux and TR rate, as shown in Fig. 8(c). It is evident that the overall forward and backward heat fluxes, as well as the TR rate, do not significantly change with an increase in W. The internal PDOS of the PCNT was calculated using Eq. (6), and the results are presented in Fig. 9(b). It can be seen that the PDOS curve varies very little with diameter. The spectral heat flux, shown in Fig. 9(d), further confirms that the PCNT heat flux is not sensitive to changes in diameter.

3.3. Effect of defects

During the fabrication of nanomaterials, randomly distributed point defects usually appear in the model, significantly affecting the heat transfer properties of the material. Therefore, it is of great research importance to study the effect of point defect concentration. The parameter ρ is introduced as the defect density, defined as the number of point defects N_{defect} as a percentage of the total number of atoms N in the model

$$\rho = \frac{N_{\text{defect}}}{N} \times 100\%. \tag{12}$$

In the models we have studied, defects are likely to appear in the left part (undoped region) or the right part (doped region), which may affect the heat flux differently and are therefore discussed separately. The concentration of defects is denoted by ρ_{L} when they appear randomly only in the left part of the model, by ρ_{R} when they appear randomly only in the right part, and by ρ_{all} when they are randomly distributed throughout the model. Here N denotes the total number of atoms in the PCNT. The effect of defect concentration on heat flux and TR rate is calculated for these three cases, as shown in Fig. 10. It can be seen that the heat fluxes in the three cases do not vary monotonically with increasing defect density.

Comparison of the effects of ρ_{L} and ρ_{R} on heat flux is shown in Figs. 10(a) and 10(b). The forward heat flux increases steadily with increasing ρ_{L} when $\rho_{\text{L}} < 0.3\%$, but first increases and then decreases when $\rho_{\text{L}} > 0.3\%$. In contrast, when the defects are distributed only on the right side, both forward and backward heat fluxes decrease to varying degrees as the defect concentration rises. Figure 10(c) shows the effect of overall defect concentration on heat flux, which exhibits an overall trend of increasing and then decreasing.

To investigate the impact of defect concentration on the sudden increase effect of heat flux (Fig. 10(a)), we separately calculated the out-of-plane PDOS at various concentrations. Additionally, to measure the PDOS overlap relationship, according to Dong *et al.*[51] and Diao *et al.*,[52] we calculated the cumulative correlation factor (CCF) for out-of-plane PDOS using the following equation, and the results are shown in Fig. 11.

$$\text{CCF}_{ij}(\omega_{\text{s}}) = \frac{\int_0^{\omega_{\text{s}}} D_i(\omega) \cdot D_j(\omega)\,\text{d}\omega}{\int_0^{\infty} D_i(\omega)\,\text{d}\omega \int_0^{\infty} D_j(\omega)\,\text{d}\omega}, \tag{13}$$

where i and j represent individual groups of atoms, and $\text{CCF}_{ij}(\omega_{\text{s}})$ is the CCF of PDOS below a specific frequency ω_{s} between i and j.

As observed in Figs. 10(a)–10(c), when defects are randomly doped only on the left side, the PDOS on the right side remains largely unchanged, while the PDOS on the left side exhibits a decreasing trend overall. Analysis of the cumulative correlation factor reveals that the PDOS overlap between the left and right sides first increases and then decreases as the defect concentration rises. This trend aligns with the observed variation in heat flux, indicating that the degree of PDOS overlap between the two sides correlates with changes in heat flux

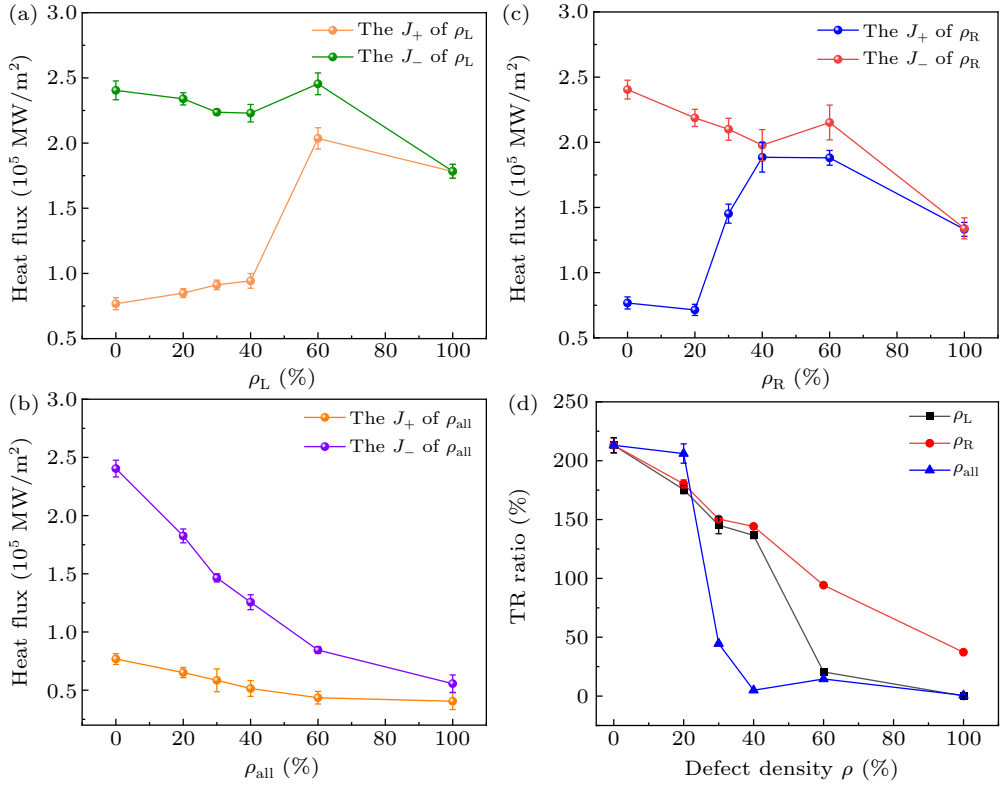


Fig. 10. Heat flux as a function of defect concentration for (a) ρ_{L}, (b) ρ_{R}, and (c) ρ_{all}, and (d) corresponding TR ratio.

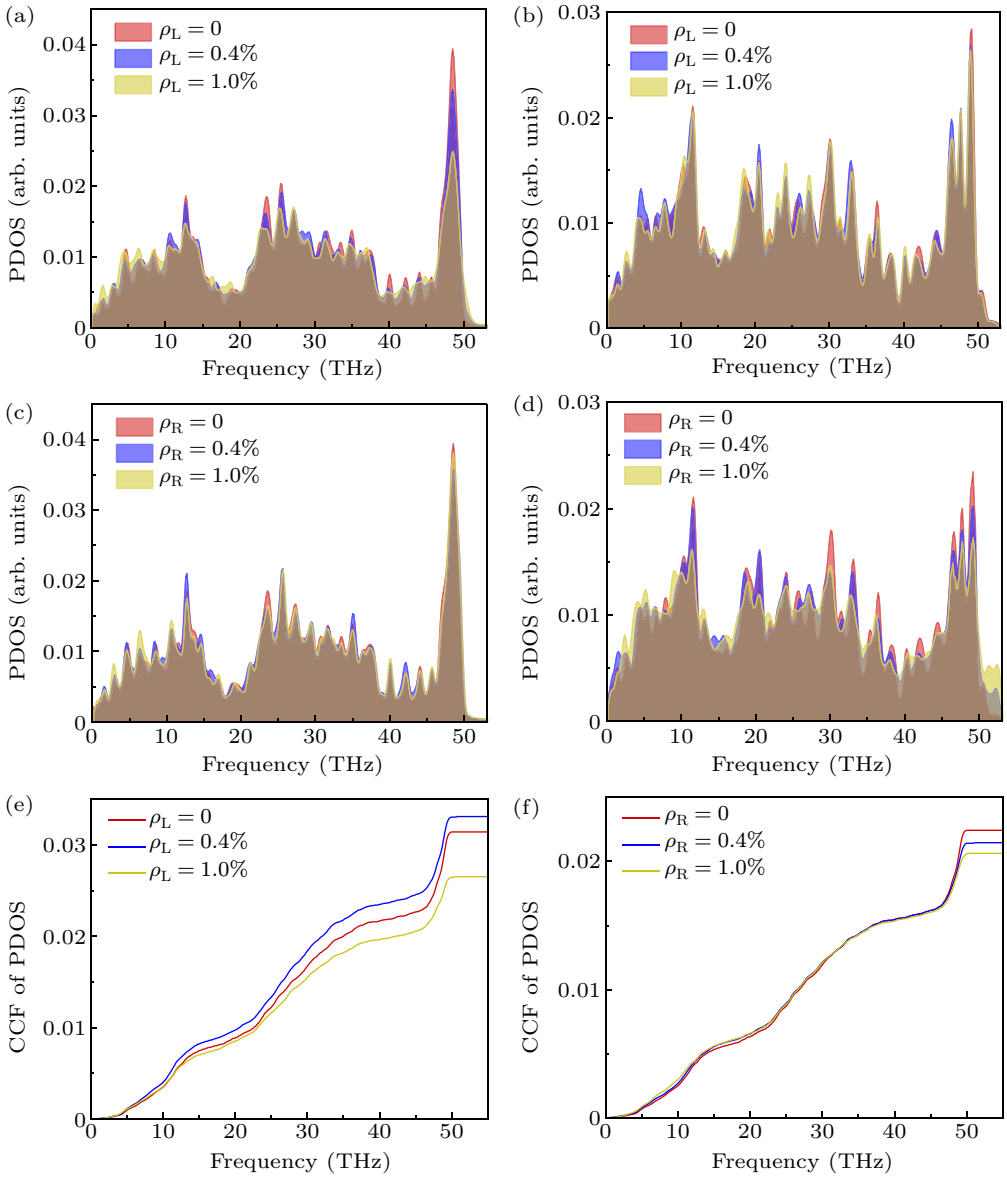


Fig. 11. Comparison of PDOS for (a) region A and (b) region B of PCNT with $\rho_L = 0$, 0.4%, and 1.0%; comparison of PDOS for (c) region A and (d) region B of PCNT with $\rho_R = 0$, 0.4%, and 1.0%; cumulative correlation factor (CCF) of PDOS curves for PCNT atoms in (e) $\rho_L = 0$, 0.4%, and 1.0%, and (f) $\rho_R = 0$, 0.4%, and 1.0%.

induced by defect doping. For ρ_L, a low defect concentration weakens the thermal conductivity of the left undoped region slightly, reducing the difference in thermal properties between the two sides, which increases the PDOS overlap and decreases the interfacial thermal resistance, leading to a rise in heat flux. However, when the defect concentration is too high, the left side is excessively weakened, increasing the PDOS mismatch again and reducing the heat flux.

As seen in Figs. 11(d)–11(f), when defects are only introduced on the right side, the PDOS on the left remains essentially unchanged, and the PDOS on the right side decreases slightly. The originally poorer thermal conductivity of the doped region combined with additional defects enhances the mismatch in the phonon spectrum, reducing heat flux. However, this weakening effect is not significant because the nitrogen doping on the right-hand side dominates phonon scattering, and the effect of additional point defects is relatively minor.

In summary, we can infer the effect of ρ_{all} on the heat flux. When defects appear randomly on both the left and right sides of the model, the thermal properties of the left region weaken faster than the right side because the undoped region is more sensitive to defects. As a result, the overall difference in heat transfer capacity between the two sides decreases, increasing the heat flux. If the defect concentration is too high, the thermal conductivity of the left region becomes lower than that of the right region. This increases the phonon spectral mismatch, thereby weakening the heat flux. As shown in Fig. 10(d), regardless of the defect location, the defect concentration exerts a strong inhibitory effect on the rectification capability of the model. This is attributed to the defects weakening the asymmetry of the forward and backward heat fluxes, and should therefore be minimized during the synthesis of the model.

4. Conclusion

In this study, we simulated three different nitrogen-doped CNT heterojunctions: PCNT, MCNT, and VCNT. The results show that PCNT exhibits superior TR efficiency at room temperature, which decreases with increasing temperature, and the TR mechanism is verified through PDOS and phonon dispersion analysis. Furthermore, a comparison between ZPCNT and APCNT highlights that although ZPCNT possesses superior rectification efficiency, it has a lower forward heat flux, while APCNT shows the opposite trend. The PPR versus phonon dispersion reveals that ZPCNT has a flatter dispersion profile and a significantly lower group velocity compared to APCNT across almost the entire frequency range.

Subsequently, we explored the effect of size on the TR rate of PCNT. Analysis of spectroscopic heat flux and PDOS reveals that increasing length excites more low-frequency phonons inside PCNT and intensifies phonon scattering at nitrogen atoms. The competition between these mechanisms results in asynchronous growth of forward and backward heat fluxes, yielding an extremely high TR rate at an intermediate length of 12 nm. In contrast, the model diameter has negligible impact on heat flux.

Finally, the effect of defect density on the TR ratio was investigated. As defect concentration increases, the heat flux exhibits a non-monotonic behavior, first increasing and then decreasing. This phenomenon is explained by the interplay between the change in thermal conductivity differences between the two sides of the model and phonon scattering at defect sites, analyzed via the overlap of PDOS on both sides. These findings provide valuable insights for the design of PCNT-based high-efficiency thermal rectifiers.

Acknowledgments

This work was supported by the National Natural Science Foundation of China (Grant No. 52476071) and the Natural Science Foundation of Hebei Province (Grant No. A2024502008).

References

[1] Starr C 1936 *Phys. Rev.* **7** 15
[2] Li N, Ren J, Wang L, Zhang G, Hänggi P and Li B 2012 *Rev. Mod. Phys.* **84** 1045
[3] Ding Y F, Zhu G M, Shen X Y, Bai X and Li B W 2022 *Chin. Phys. B* **31** 126301
[4] Li B, Wang L and Casati G 2004 *Phys. Rev. Lett.* **93** 184301
[5] Yang X, Wang S, Wang C, Lu R, Zheng X, Zhang T, Liu M, Zheng J and Chen H 2022 *ACS Appl. Mater. Interfaces* **14** 4434
[6] Maleki H, Fischer T, Bohr C, Auer J, Mathur S and Milow B 2021 *Biomacromolecules* **22** 1739
[7] Ma R, Wu D, Liu Y, Ye H and Sutherland D 2020 *Mater. Des.* **188** 108407
[8] Li Y, Li J, Qi M, Qiu C W and Chen H 2021 *Phys. Rev. B* **103** 014307
[9] Terraneo M, Peyrard M and Casati G 2002 *Phys. Rev. Lett.* **88** 094302
[10] Chen X K, Pang M, Chen T, Du D and Chen K Q 2020 *ACS Appl. Mater. Interfaces* **12** 15517
[11] Chen X, Xie Z, Zhou W, Tang L and Chen K 2016 *Carbon* **100** 492
[12] Wu N, Liu Y, Wang S, Xing Z, Li H and Li X 2024 *Int. J. Heat Mass Transfer* **221** 125097
[13] Wang Y, Chen S and Ruan X 2012 *Appl. Phys. Lett.* **100** 163101
[14] Yang B, Li D, Qi L, Li T and Yang P 2019 *Phys. Lett. A* **383** 1306
[15] Gordiz K and Vaez Allaei S M 2014 *J. Appl. Phys.* **115** 163512
[16] Lee J, Varshney V, Roy A K, Ferguson J B and Farmer B L 2012 *Nano Lett.* **12** 3491
[17] Zhang Z, Chen Y, Xie Y and Zhang S 2016 *Appl. Therm. Eng.* **102** 1075
[18] Liu B, Baimova J A, Reddy C D, Dmitriev S V, Law W K, Feng X Q and Zhou K 2014 *Carbon* **79** 236
[19] Chen X K, Liu J, Xie Z X, Zhang Y, Deng Y X and Chen K Q 2018 *Appl. Phys. Lett.* **113** 121906
[20] Liu Y Y, Zhou W X, Tang L M and Chen K Q 2014 *Appl. Phys. Lett.* **105** 051905
[21] Gordiz K, Vaez Allaei S and Kowsary F 2011 *Appl. Phys. Lett.* **99** 251901
[22] Zhang T and Luo T 2015 *Small* **11** 4657
[23] Cottrill A L, Wang S, Liu A T, Wang W J and Strano M S 2018 *Adv. Energy Mater.* **8** 1702692
[24] Iijima S 1991 *Nature* **354** 56
[25] Aiyiti A, Zhang Z, Chen B, Hu S, Chen J, Xu X and Li B 2018 *Carbon* **140** 673
[26] Chen X K, Xie Z X, Zhang Y, Deng Y X, Zou T H, Liu J and Chen K Q 2019 *Carbon* **148** 532
[27] Zhuang S and Liu Y 2020 *J. Phys. Chem. Lett.* **11** 9731
[28] Yang P, Li X, Yang H, Wang X, Tang Y and Yuan X 2013 *Appl. Phys. A* **112** 759
[29] Chien S K and Yang Y T 2010 *Phys. Lett. A* **374** 4885
[30] Zhang X, Han G and Zhu S 2024 *Small* **20** 2305406
[31] Guo L R, Song K B, Li Y J and Li Y G 2023 *Acta Phys. Sin.* **72** 013102 (in Chinese)
[32] Plimpton S 1995 *J. Comput. Phys.* **117** 1
[33] Ghasemi H, Abraham B, Rutledge J and Yazdani H 2020 *Diamond Relat. Mater.* **109** 108090
[34] Cheng X and Wang X 2019 *Nanotechnology* **30** 255401
[35] Melchionna S, Ciccotti G and Holian B L 1993 *Mol. Phys.* **78** 533
[36] Berendsen H J, Postma J V, Van Gunsteren W F, DiNola A and Haak J R 1984 *J. Chem. Phys.* **81** 3684
[37] Song J, Xu Z and He X 2020 *Int. J. Heat Mass Transfer* **157** 119954
[38] Farzadian O, Razeghiyadaki A, Spitas C and Kostas K 2020 *Nanotechnology* **31** 485401
[39] Le M Q 2014 *Meccanica* **49** 1709
[40] Ma D, Wan X and Yang N 2018 *Phys. Rev. B* **98** 245420
[41] Liang T, Zhou M, Zhang P, Yuan P and Yang D 2020 *Int. J. Heat Mass Transfer* **151** 119395
[42] Wang Y, Vallabhaneni A, Hu J, Qiu B, Chen Y P and Ruan X 2014 *Nano Lett.* **14** 592
[43] Yang N, Zhang G and Li B 2009 *Appl. Phys. Lett.* **95** 033107
[44] Chen J, Zhang G and Li B 2010 *Nano Lett.* **10** 3978
[45] Jiang P, Hu S, Ouyang Y, Ren W, Yu C, Zhang Z and Chen J 2020 *J. Appl. Phys.* **127** 235101
[46] Wu N, Liu Y, Wang S and Xing Z 2024 *ACS Appl. Mater. Interfaces* **16** 9155
[47] Chen X K, Liu J, Xie Z X, Zhang Y, Deng Y X and Chen K Q 2018 *Appl. Phys. Lett.* **113** 121906
[48] Sääskilahti K, Oksanen J, Tulkki J and Volz S 2014 *Phys. Rev. B* **90** 134312
[49] Ma Y, Zhang Z, Chen J, Sääskilahti K, Volz S and Chen J 2018 *Carbon* **135** 263
[50] Sha W, Dai X, Chen S and Guo F 2022 *Diamond Relat. Mater.* **129** 109341
[51] Dong Y, Diao C, Song Y, Chi H, Singh D J and Lin J 2019 *Phys. Rev. Appl.* **11** 024043
[52] Diao C, Yang Z, Dong Y and Duan Y 2020 *Int. J. Heat Mass Transfer* **157** 119851